



Cite this: *Mater. Adv.*, 2022, **3**, 4890

# Dielectric properties correlation with microstructure in $\text{ABi}_4\text{Ti}_4\text{O}_{15}$ (A = Sr, Ba) bismuth layered ferroelectrics

Vipul Kumar Sharma, <sup>a</sup> Rashi Nathawat <sup>a</sup> and Satyapal S. Rathore <sup>\*ab</sup>

The bismuth layered ferroelectrics (BLFs)  $\text{BaBi}_4\text{Ti}_4\text{O}_{15}$  and  $\text{SrBi}_4\text{Ti}_4\text{O}_{15}$  were synthesized using solid-state-reaction technique and the impact of 'thermal etching' on their microstructure and dielectric and ferroelectric properties was thoroughly investigated. The phase formation and crystallization to the orthorhombic  $A2_1am$  phase was confirmed by XRD followed by Rietveld refinement. The thermally etched compounds depict the formation of highly uniform plate-like grain distribution with a reduced grain size. The effect of improved microstructure was also evident in the dielectric properties with a colossal change in the dielectric constant,  $\epsilon'$ . Furthermore, the study suggests that the ferroelectric polarization can also be improved by thermal etching, reducing the contribution due to non-ferroelectric components. The impedance analysis using a brick-layer model shows that impedance is predominantly due to grains (bulk) with a relatively small contribution due to grain boundaries in these BLFs. The observed change in macroscopic properties was attributed to the modification in grain-grain boundary configuration post thermal etching.

Received 23rd March 2022,  
Accepted 24th April 2022

DOI: 10.1039/d2ma00333c

rsc.li/materials-advances

## 1 Introduction

Piezoelectric devices have been an integral part of our technological evolution due to their extensive applications in consumer electronics, aerospace, defence, health monitoring, scientific equipment and many others.<sup>1–4</sup> However, the majority of these devices utilize ceramic piezoelectrics, which in turn are predominantly Pb-based piezoelectric systems.<sup>5–11</sup> The long term adverse impact of Pb on the human body and environment due to a lack of appropriate disposal has been raised by organizations such as the WHO and RoHS from time to time.<sup>12,13</sup> Due to the utility of piezoelectric devices, the development of eco-friendly alternatives to Pb-based piezoelectric materials with comparable device performances can be considered one of the most urgent challenges faced by the scientific community. Thus, the search for Pb-free piezoelectric systems to develop clean and sustainable technology has seen an upsurge in the last decade.<sup>14,15</sup> One of the promising piezoelectric systems to envisage Pb-free devices in the future is the Aurivillius family of compounds. The piezo-properties of these compounds were observed to be inferior when compared with their Pb-based counterparts. However, due to

their high Curie temperature, large dielectric constant, low losses and excellent thermal and chemical stability they have emerged as potential candidates for high temperature piezo-electric applications. In addition, many compounds in these Pb-free ceramics also possess a relaxor ferroelectric state with a good piezo-response, which makes them an ideal system to be used over a temperature range as their dielectric constant remains maximum in a wide temperature window.<sup>16–21</sup>

The Aurivillius family of compounds, also known as bismuth layered ferroelectrics (BLFs) is represented by  $[\text{Bi}_2\text{O}_2]^{2+}[\text{A}_{m-1}\text{B}_m\text{O}_{3m+1}]^{2-}$ . Here A is mono, di, or trivalent or their mixture, B is tetravalent, pentavalent or their mixture of elements, and  $m = 1, 2, 3, 4$  or  $5$ . Due to a large possible combination of A and B sites as well as  $m$ , many derivatives of BLFs have been reported in the literature.<sup>22</sup> Interestingly, the piezo-properties of this system have shown significant dependence on the partial and complete substitution at the A, B and Bi sites. Moreover, ion substitution is one of the most common approaches to introduce new functionalities such as magnetic order in these complex oxides.<sup>23</sup> Furthermore, the physical properties of these oxides were observed to show dependence on the synthesis conditions and processing parameters. Thus, the Pb-free Aurivillius family of compounds possesses excellent dielectric and piezoelectric properties, which can be tailored by controlling the synthesis conditions, processing parameters and ionic substitutions based on crystal chemical principles. Therefore, careful control of these parameters becomes essential

<sup>a</sup> Functional Ceramics and Smart Materials Lab, Department of Physics, Manipal University Jaipur, Jaipur, 303007, India. E-mail: satyapal03@gmail.com; Tel: +91-9930437849

<sup>b</sup> Department of Physics, Cluster University of Jammu, Jammu, Jammu & Kashmir, 180001, India



to achieve the reproducibility of functional properties for any specific application.

In the present work, an attempt is made to understand the effect of one such processing parameter, thermal etching, on the structural, dielectric and piezo-electric properties of  $\text{BaBi}_4\text{Ti}_4\text{O}_{15}$  and  $\text{SrBi}_4\text{Ti}_4\text{O}_{15}$ . These two isomorph complex oxides were chosen as they possess contrasting dielectric responses conforming to relaxor ferroelectric and normal ferroelectric phases respectively. Thus their dielectric properties cover a wide spectrum of bismuth layered ferroelectric systems. A highly uniform plate-like microstructure (typical of BLFs) was observed for both the phases post thermal etching, with a significant variation in dielectric and piezoelectric properties. To understand a correlation between the microstructure and macroscopic properties, a brick layer model has been proposed which could be utilized to understand the dielectric properties of the Aurivillius family of compounds in general.

## 2 Experimental details

The polycrystalline  $\text{BaBi}_4\text{Ti}_4\text{O}_{15}$  (BBT) and  $\text{SrBi}_4\text{Ti}_4\text{O}_{15}$  (SBT) were synthesized using a solid state reaction technique. Initially, highly pure  $\text{BaCO}_3/\text{SrCO}_3$ ,  $\text{Bi}_2\text{O}_3$  and  $\text{TiO}_2$  were ground in an agate mortar and pestle. The precursor mixture to synthesize BBT was calcined for 4 h at  $800^\circ\text{C}$  followed by intermediate grinding of the powder and recalcination at  $950^\circ\text{C}$  for 8 h. On the other hand, the initial precursor mixture to synthesize SBT was calcined at  $900^\circ\text{C}$  for 3 h. The single phase powders of both materials were pressed into pellets of 10 mm in diameter and 2 mm thickness using polyvinyl alcohol (PVA) as the binder. The 'green' pellets of both materials were then sintered at  $1100^\circ\text{C}$  for 2 h and named the 'as-sintered' (AS) pellet in the present work. These as-sintered pellets of both materials were mirror polished with  $\text{Al}_2\text{O}_3$  abrasive of size  $0.5\ \mu\text{m}$  using BUEHLER polisher. These fine polished pellets were then heat treated at  $1030^\circ\text{C}$  for 30 minutes in a high temperature furnace and called 'thermally-etched' (TE) pellets in the current study.

The room temperature crystal structure study was performed using a Bruker D8 Advance X-ray diffractometer with  $\text{Cu-K}\alpha$  radiation of  $1.54\ \text{\AA}$ . The microstructural study was performed with a JEOL make JSM-7610F Plus FESEM. The high temperature (RT to 923 K) dielectric measurements for the AS and TE pellets of both materials were performed at various frequencies (1 Hz to 10 MHz) using a Novocontrol, Concept – 80 broadband dielectric spectrometer. Furthermore, the  $P$ - $E$  loop measurements were carried out with an AIXACCT  $P$ - $E$  loop analyser.

## 3 X-ray diffraction studies

The room temperature powder X-ray diffraction patterns for  $\text{BaBi}_4\text{Ti}_4\text{O}_{15}$  and its isomorph  $\text{SrBi}_4\text{Ti}_4\text{O}_{15}$  are shown in Fig. 1(b) and (c) respectively. The Rietveld refinement reveals that both Aurivillius compounds crystallize in the orthorhombic (pseudo-tetragonal) phase conforming to a non-centrosymmetric  $A2_1am$

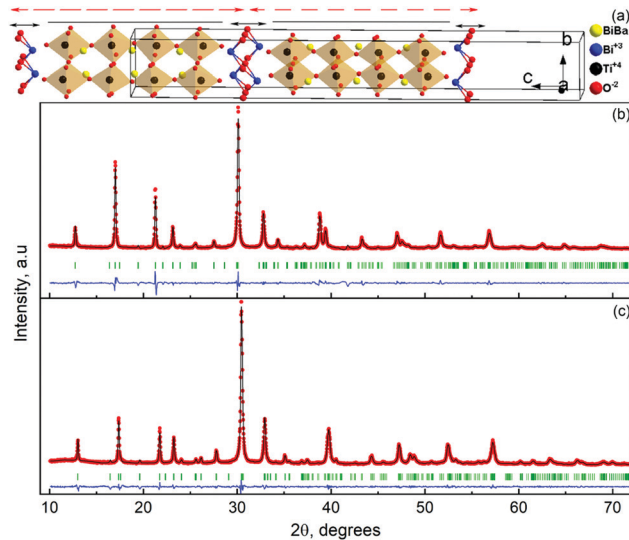


Fig. 1 (a) The crystal structure of  $\text{BaBi}_4\text{Ti}_4\text{O}_{15}$  viewed along the  $[001]$  direction ( $z = -0.25$  to  $z = 0.75$ ); for details please refer to the text. The Rietveld plot for (b)  $\text{BaBi}_4\text{Ti}_4\text{O}_{15}$  and (c)  $\text{SrBi}_4\text{Ti}_4\text{O}_{15}$  obtained by structure refinement in the orthorhombic space group  $A2_1am$ . The observed data, calculated pattern and difference plot are shown by the red circle, black line through a circle and blue line at the bottom respectively. The green vertical bars indicate the allowed Bragg reflections.

space group symmetry ( $Z = 2$ ). Previous studies have shown a possibility of both  $\text{BaBi}_4\text{Ti}_4\text{O}_{15}$  and  $\text{SrBi}_4\text{Ti}_4\text{O}_{15}$  existing in tetragonal  $I_4/mmm$  symmetry, due to nearly the same values of in plane ( $a$ - $b$ ) lattice parameters ' $a$ ' and ' $b$ '.<sup>24</sup> The ratio of these lattice parameters was observed in the present study to be 1.0006 and 1.001 for  $\text{BaBi}_4\text{Ti}_4\text{O}_{15}$  and  $\text{SrBi}_4\text{Ti}_4\text{O}_{15}$  respectively. Due to similar values of ' $a$ ' and ' $b$ ', all the reflections in the powder X-ray diffraction pattern could also be associated with the centrosymmetric tetragonal structure. However, previous high-resolution synchrotron XRD and selected area electron diffraction studies revealed the presence of Bragg reflections which are forbidden by tetragonal symmetry<sup>25</sup> and hence the existence of both Aurivillius compounds in an orthorhombic phase.

Thus, in the current study, initially both  $A2_1am$  and  $I_4/mmm$  symmetries were modelled for refinement, and both compounds show a slightly better value of  $\chi^2$  for  $A2_1am$ . The calculated pseudo-tetragonal values  $a_T = \frac{(a+b)}{2\sqrt{2}}$  for  $\text{BaBi}_4\text{Ti}_4\text{O}_{15}$  and  $\text{SrBi}_4\text{Ti}_4\text{O}_{15}$  are 3.863 and 3.847 respectively, which are in good agreement with the literature.<sup>26</sup> The Rietveld plot for both compounds shows the absence of any unaccounted diffraction peak; and all reflections could be indexed to an orthorhombic structure, indicating the synthesized ceramics are in the single phase. The structure refinement parameters are summarized in Table 1, and indicate a good fit between the observed and calculated pattern. The refinement demonstrates an expected decrease in all the dimensional lattice parameters, ' $a$ ', ' $b$ ', and ' $c$ ' of SBT, for relatively smaller  $\text{Sr}^{2+}$  ion substitution at the  $\text{Ba}^{2+}$  site. The result of this study is in good agreement with the literature.<sup>27</sup>

The crystal structure of the bismuth-layered Aurivillius phase is shown in Fig. 1(a). A unit cell contains two formula



**Table 1** The crystallographic parameters obtained from refinement of the room temperature diffraction pattern for BaBi<sub>4</sub>Ti<sub>4</sub>O<sub>15</sub> and SrBi<sub>4</sub>Ti<sub>4</sub>O<sub>15</sub>. The structural parameters for SrBi<sub>4</sub>Ti<sub>4</sub>O<sub>15</sub> are shown in square brackets []. The lattice and profile parameters are shown at the bottom of the table

Atom	Wyc.	<i>x</i>	<i>y</i>	<i>z</i>	Occup
Bi <sub>1</sub>	4a	0.1186(7)[0.1313(5)]	0.3852(3)[0.3786(7)]	0.00000	0.50
Ba <sub>1</sub> [Sr <sub>1</sub> ]	4a	0.1186(7)[0.1313(5)]	0.3852(3)[0.3786(7)]	0.00000	0.50
Bi <sub>2</sub>	8b	0.5403(7)[0.5415(1)]	0.2306(5)[0.2756(1)]	0.2248(2)[0.2239(9)]	1.00
Bi <sub>3</sub>	8b	0.1765(8)[0.1569(7)]	0.2855(4)[0.2812(4)]	0.9008(5)[0.9005(8)]	0.75
Ba <sub>2</sub> [Sr <sub>2</sub> ]	8b	0.1765(8)[0.1569(7)]	0.2855(4)[0.2812(4)]	0.9008(5)[0.9005(8)]	0.25
Ti <sub>1</sub>	8b	0.3553(1)[0.2852(5)]	0.4730(4)[0.4474(5)]	0.5709(7)[0.5752(4)]	1.00
Ti <sub>2</sub>	8b	0.5462(7)[0.5421(5)]	−0.2780(6)[−0.267(1)]	0.3449(6)[0.3456(4)]	1.00
O <sub>1</sub>	4a	0.6030(8)[0.5703(2)]	0.1951(9)[0.2107(4)]	0.00000	1.00
O <sub>2</sub>	8b	0.2378(1)[0.2378(5)]	0.3120(8)[0.3120(7)]	0.4156(2)[0.4156(2)]	1.00
O <sub>3</sub>	8b	0.3805(4)[0.3509(5)]	0.0344(8)[−0.0018(2)]	0.5564(2)[0.5511(3)]	1.00
O <sub>4</sub>	8b	0.5463(5)[0.5613(2)]	0.2733(4)[0.3398(3)]	0.2684(9)[0.2755(8)]	1.00
O <sub>5</sub>	8b	0.4174(3)[0.4174(2)]	0.4672(2)[0.4672(7)]	0.4486(8)[0.4486(6)]	1.00
O <sub>6</sub>	8b	0.2220(3)[0.2220(3)]	0.2448(6)[0.2448(7)]	0.4148(6)[0.4148(7)]	1.00
O <sub>7</sub>	8b	0.4053(7)[0.4332(7)]	0.1238(2)[0.1524(1)]	0.3440(8)[0.3452(5)]	1.00
O <sub>8</sub>	8b	0.2577(4)[0.2495(3)]	0.3258(9)[0.1817(6)]	0.6514(5)[0.6511(3)]	1.00
	BaBi <sub>4</sub> Ti <sub>4</sub> O <sub>15</sub>	SrBi <sub>4</sub> Ti <sub>4</sub> O <sub>15</sub>			
<i>a</i>	5.4655(3) Å	5.4445(3) Å			
<i>b</i>	5.4621(2) Å	5.4371(2) Å			
<i>c</i>	41.788(5) Å	40.911(3) Å			
$\alpha = \beta = \gamma$	90°	90°			
Space group	A2 <sub>1</sub> am (39)	A2 <sub>1</sub> am (39)			
$\chi^2$ , <i>R</i> <sub>p</sub> and <i>R</i> <sub>WP</sub>	1.58, 14.1 and 16.3	1.43, 12.2 and 13.3			
2 $\theta$ , X-ray source	10° to 100°, Cu K $\alpha$	10° to 100°, Cu K $\alpha$			

units of BaBi<sub>4</sub>Ti<sub>4</sub>O<sub>15</sub>. The crystal structure can be best represented when viewed from [001]. From *z* = −0.25 to 0.75 it shows two units of BaBi<sub>4</sub>Ti<sub>4</sub>O<sub>15</sub>, indicated by the dotted two-headed arrow. This unit (*z* = 0.25 to 0.75) can be further divided into four (*m* = 4) perovskite-like units of (BaBi) TiO<sub>3</sub>, with the overall composition of BaBi<sub>2</sub>Ti<sub>4</sub>O<sub>13</sub> (shown by the solid line). These perovskite-like units are sandwiched between Bi<sub>2</sub>O<sub>2</sub> layers along the pseudo-tetragonal *c*-axis (designated as a solid double-sided arrow), giving it the characteristic name of bismuth layered structures. The 4a and 8b sites between the perovskite-like units are partially occupied by Bi and Ba, with site occupancy of 50% each (4a) and 75% and 25% (8b) respectively. The bismuth layered structure is attributed to the Bi<sub>2</sub> (8b) site completely occupied by Bi<sup>3+</sup> ions.

## 4 Microstructural analysis

The FESEM electron photo-micrographs for BBT and SBT sintered pellets are shown in Fig. 2. A non-uniform distribution of crystallites with the presence of small (~0.1 μm) to large (~2 μm) grains can be clearly seen for the as-sintered surfaces of BBT and SBT [Fig. 2(a and d)]. However, the thermally etched pellets of synthesized oxides [Fig. 2(b and e)] show a highly uniform grain distribution. This plate-like grain morphology is a characteristic of BLF orthorhombic phases. The histograms in Fig. 2(c) and (f) show a comparative grain size distribution over the captured image for BBT and SBT oxides respectively. The statistical average grain size for BBT-AS and BBT-TE is 0.5969 μm and 0.3604 μm respectively. However, the calculated average grain size for SBT-AS and SBT-TE was obtained as 1.0683 μm and 0.4114 μm respectively. This visible enhancement in grain morphology and reduction in average grain size of the TE pellet in both materials reveals that the thermal etching is a

simple yet effective processing method to improve the microstructure of the Aurivillius family of compounds. However, the statistically calculated average grain size for SBT was observed to be greater than that for BBT, which indicates dependence on the A-site composition. This improvement in grain morphology can be attributed to redistribution of surface energy due to the diffusion of atoms from the grain boundary.<sup>28,29</sup>

The fundamental theory of crystallization may give some insight to understanding the growth of the observed random plate-like grains in both materials.<sup>30</sup> The BBT and SBT both have a bismuth layered structure with stacking of four perovskite-like units sandwiched between the layer of bismuth oxide (Bi<sub>2</sub>O<sub>2</sub>) [Fig. 1(a)] along the *c*-axis. This is the reason for the large value of lattice constant '*c*' (7.5 times) when compared with '*a*' and '*b*'. All the crystal unit cells assemble themselves along crystallographic axes during heat treatment and a large array of unit cells then forms a grain. The layered axis was observed to be the hard growing direction whereas *a* and *b* are relatively easy growing axes.<sup>31</sup> This results in the observed typical pellet-like grains with a very small breadth (*c*-axis) compared to its length (*a* and *b* axes).

## 5 Dielectric studies

The temperature-dependent (30 °C to 700 °C) dielectric response (real part of the dielectric constant,  $\epsilon'$ ) at discrete frequencies (1 Hz to 1 MHz) for the synthesized compounds is shown in Fig. 3. The AS and TE BBT exhibit a typical relaxor ferroelectric transition with peak maxima, *T*<sub>m</sub> shifting towards a higher temperature with an increase in frequency. The ferroelectric, broadened relaxor and paraelectric regions are shown as Region I, II and III respectively in Fig. 3(a and b). The observed diffuse phase transition and variation of *T*<sub>m</sub> from 410 °C to 390 °C in the measured frequency range is in good



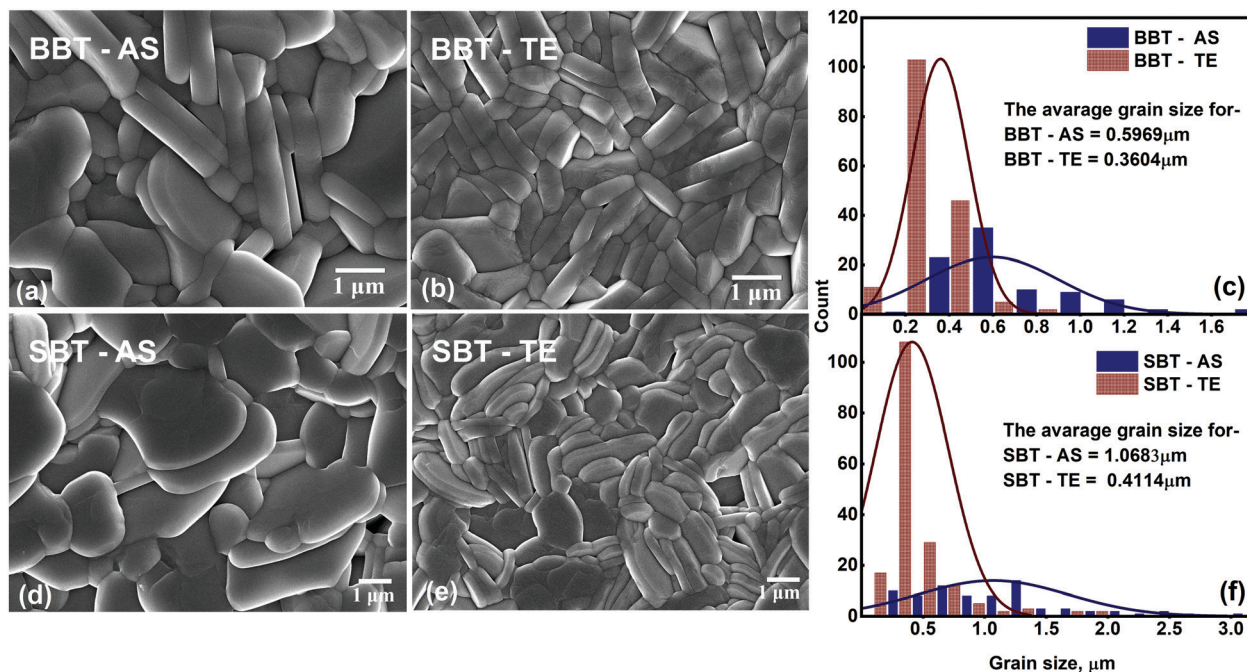


Fig. 2 The scanning electron photomicrograph for (a) BBT-AS, (b) BBT-TE, (d) SBT-AS and (e) SBT-TE along with the statistical grain size distribution curve for (c) BBT and (f) SBT. The continuous grey and blue lines in the distribution curve represent the distribution over the histogram, and do not represent any mathematical relation.

agreement with the literature.<sup>32–34</sup> Both AS and TE BBT transform into the *para*-electric state at identical temperatures, whereas an observable increase in value of the dielectric constant ( $\Delta\epsilon'_m$  30%) is observed in the measured frequency region. The observed diffused phase transition in BBT is usually attributed to the presence of Polar Nano Regions (PNRs).<sup>35</sup> These isolated domains start to grow as the temperature is reduced and below  $T_m$  transform into a long range ferroelectric state of highly correlated PNRs. Thus, a modified Curie-Weiss law is used to understand the dynamic nature of the dielectric relaxation:<sup>36,37</sup>

$$\frac{1}{\epsilon'} - \frac{1}{\epsilon_m} = \frac{(T - T_m)^\gamma}{C} \quad (1)$$

where  $C$  is the Curie-Weiss constant,  $\epsilon_m$  is the maximum value of the dielectric constant at  $T_m$ ,  $T$  is the temperature and  $\gamma$  is the critical exponent (degree of diffuseness). The value of  $\gamma$  ranges  $1 \leq \gamma \leq 2$ , where  $\gamma = 1$  represents a normal ferroelectric,  $\gamma > 1$  represents a relaxor state and  $\gamma = 2$  indicates perfect relaxors. The degree of diffuseness was observed to be slightly higher in TE BBT (1.5) compared to AS BBT (1.49), an effect of smaller and uniform grain size distribution.

The similarities observed in the structural properties of BBT and SBT ends here as SBT shows a frequency independent ferro to paraelectric 1st order phase transition (Fig. 3(c) and (d)). Thus, substituting  $\gamma = 1$  for normal ferroelectrics, eqn (1) reduces to the Curie-Weiss law.<sup>38</sup>

$$\frac{1}{\epsilon'} - \frac{1}{\epsilon_c} = \frac{T - T_c}{C} \quad (2)$$

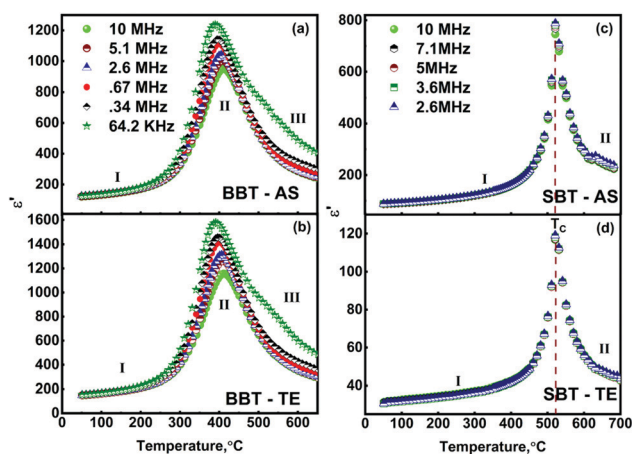


Fig. 3 The temperature dependent dielectric constant at discrete frequencies for (a) As sintered-BBT, (b) thermally etched-BBT, (c) as sintered-SBT and (d) thermally etched-SBT. (c and d) show a large change in the dielectric constant for AS SBT and TE SBT, and also the transition temperature is independent of applied AC field frequencies.

where  $T_c$  is the ferroelectric transition temperature and  $\epsilon_c$  is the maximum value of the dielectric constant at  $T_c$ . The fitting with the above equation (not shown) indicates that both AS and TE SBT transform from the tetragonal (centrosymmetric) to orthorhombic (non-centrosymmetric) ferroelectric state below 521 °C. Surprisingly, in contrast to BBT, the TE SBT exhibits a large reduction in dielectric constant (6.5 times) compared to AS SBT. This extremely large change in bulk dielectric constant by a single processing step is remarkable.



Table 2 A summarized table of extracted values from a modified Curie-Weiss and Curie-Weiss relation for BBT and SBT pellets respectively

BBT						SBT					
Frequency	As-sintered		Thermally etched		Difference	Frequency	As sintered		Thermally etched		Difference
	$T_m$	$\epsilon'_m$	$T_m$	$\epsilon'_m$	$\Delta\epsilon'_m$		$T_c$	$\epsilon'_c$	$T_c$	$\epsilon'_c$	$\Delta\epsilon'_c$
10 MHz	410	949.9	410	1156.3	206.4	10 MHz	521	745.46	521	116.80	628.66
5.1 MHz	405	1000.7	405	1261.6	260.9	7.1 MHz	521	768.34	521	117.19	651.15
2.6 MHz	405	1038.7	405	1309.7	271	5 MHz	521	775.55	521	117.409	658.14
0.67 MHz	400	1111.82	400	1416.08	304.26	3.6 MHz	521	781.85	521	118.21	663.64
0.34 MHz	395	1142.57	395	1456.98	314.41	2.6 MHz	521	788.05	521	119.11	668.94
64.2 kHz	390	1237.04	390	1578.16	341.12	—	—	—	—	—	—

The two interesting observations in dielectric studies are as follows:

1. The complete substitution at the Ba site in  $\text{BaBi}_4\text{Ti}_4\text{O}_{15}$  with Sr exhibits a transformation from relaxor ferroelectric state to a normal ferroelectric state.

2. The thermal etching post sintering enhances the dielectric constant for  $\text{BaBi}_4\text{Ti}_4\text{O}_{15}$ , but significantly reduces it for  $\text{SrBi}_4\text{Ti}_4\text{O}_{15}$ .

The previous experimental and theoretical studies suggest that the spontaneous polarization in these BLF oxides originates due to a combination of both octahedral tilting in perovskite-like units and  $[\text{Bi}_2\text{O}_2]$  distortion.<sup>39–42</sup> However, the A site is not considered to play an important role in the origin of spontaneous dipoles. A nearly 110 °C rise in transition temperature (at 10 MHz) and 10 times reduction in dielectric constant on substituting  $\text{Ba}^{2+}$  with  $\text{Sr}^{2+}$  suggests that the A-site plays an important role in deciding the dielectric properties of these complex oxides. A similar relaxor to ferroelectric transition was observed for partial and complete Sr and Ba substitution in other functional oxides such as (Sr, Ba)  $\text{Bi}_2\text{Nb}_2\text{O}_9$  and (Sr, Ba)  $\text{TiO}_3$ .<sup>43–45</sup> The origin of relaxor behaviour and transition to the ferroelectric state is not well understood in these oxides. A plausible reason for this transformation and contrasting change in dielectric constant with thermal etching may be associated with the chemical nature of Ba and Sr. These alkaline earth metals have a comparable ionic size but different atomic masses (Ba, 137.3 and Sr, 87.62), electronic configuration (Ba,  $[\text{Xe}]6s^2$  and Sr,  $[\text{Kr}]5s^2$ ) and electronegativities (Ba, 0.9 and Sr, 1.0). Furthermore, the co-valency or some other parameters might be deciding factors for the observed dependence on non-ferroelectric sites in a variety of ferroelectric oxides. The important dielectric parameters obtained for BBT and SBT are summarized in Table 2.

## 6 Impedance analysis

The bulk (grain) and grain boundary contributions in many polycrystalline ferroelectric systems are usually demonstrated by two semicircles in the complex impedance plane ( $Z'$  vs.  $Z''$ ) at high and low frequencies respectively. However, this clear distinction between bulk and grain boundary contributions is absent in the Nyquist plot of many complex systems. Thus, to evaluate the impedance due to grains and grain-boundaries a

brick-layer formalism,<sup>46</sup> which is inspired by the observed microstructure, has been suggested (Fig. 4). The equivalent circuit has two contributive regions; (a) the first region is the surface capacitive region for the grain boundary of width  $t$ , and (b) the second region is the contribution due to grains of width  $T$  ( $t \ll T$ ). To understand the macroscopic impedance, the micro-region contributions were modelled with an equivalent circuit shown in Fig. 4(b). This circuit can be seen as a combination of two parallel  $R$ - $C$  circuits, representing the average contribution of grain and grain boundary along with resistive and capacitive elements ( $R_g, R_{gb}, C_g, C_{gb}$ ). In addition, an extra parallel Constant Phase Element (CPE) is introduced to satisfy dispersion of relaxation time with frequency. This capacity dispersion is usually attributed to surface heterogeneities, electrode porosity, slow adsorption reaction on electrodes, non-uniform potential distribution and other inhomogeneities in the polycrystalline phase.<sup>47</sup> The impedance value due to CPE is given in the below equation:

$$Z_{\text{CPE}} = \frac{1}{A_0(j\omega)^n} \quad (3)$$

where  $A_0$  is a constant related to active area,  $\omega$  is the angular frequency and  $n$  is the CPE exponent. The CPE represents a limiting behaviour of a circuit and the values of  $n = 0, 1$ , and  $-1$  indicate the purely resistive, capacitive and inductive nature

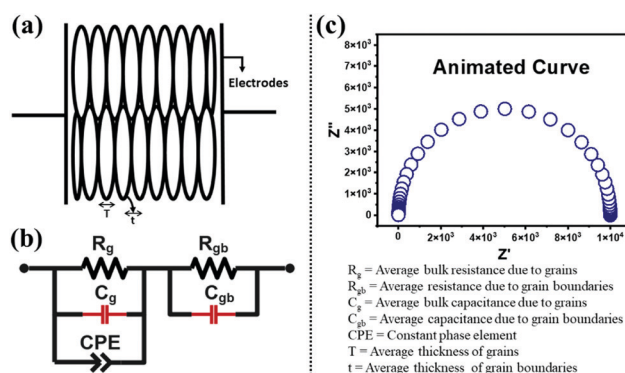


Fig. 4 (a) The brick layer model consists of plate-shaped grains to simulate the capacitive and resistive contribution by grains and grain boundaries. (b) The different components contributing to impedance and their equivalent circuit. (c) A simulated Nyquist plot is drawn as according to the equivalent circuit in the frequency range of 1 Hz to 1 MHz.



respectively. The complex impedance from the equivalent circuit was calculated using the following equations.<sup>48</sup>

$$Z^* = Z' - jZ'' = \frac{1}{R_g^{-1} + j\omega C_g + A_0(j\omega)^n} + \frac{1}{R_{gb}^{-1} + j\omega C_{gb}} \quad (4)$$

The real and imaginary part of impedance are given by:

$$Z' = \frac{(1 + C_1\omega^n)^2}{(1 + C_1\omega^n)^2 + (\omega R_g C_g + C_2\omega^n)^2} + \frac{R_{gb}}{1 + (\omega R_{gb} C_{gb})^2} \quad (5)$$

and

$$Z'' = R_g \left[ \frac{\omega R_g C_g + C_2\omega^n}{(1 + C_1\omega^n)^2 + (\omega R_g C_g + C_2\omega^n)^2} \right] + R_{gb} \left[ \frac{\omega R_{gb} C_{gb}}{1 + (\omega R_{gb} C_{gb})^2} \right] \quad (6)$$

where  $C_1 = A_0 R_g \cos\left(\frac{n\pi}{2}\right)$  and  $C_2 = A_0 R_g \sin\left(\frac{n\pi}{2}\right)$ .

To obtain an equivalent circuit corresponding to the observed Nyquist plot in the entire frequency range is challenging due to different possible contributions to impedance in the polycrystalline phase. The current approach to evaluate this

contribution using a brick-layer model is in good agreement with experimental impedance and also yields realistic values of grain and grain boundary impedance. A semi-circular arc-like Nyquist plot observed in the complex impedance plane was fitted with the simulated Nyquist plot (Fig. 4(c)). The observed impedance for all samples and their corresponding fitted curve (red solid line) are shown in Fig. 5. The lowering of impedance with an increase in temperature can be seen as a reduction in the radius of the semi-circular arc at high temperatures (Fig. 5). Some arcs at high temperature cannot be clearly seen due to the chosen axis-range. This decrease in impedance with temperature is expected due to an increase in the thermally assisted conduction mechanism in ceramic oxides.

Comparative data of the extracted values, obtained from the fitting of an equivalent circuit are presented in Table 3. The values of resistance ( $R_g$  and  $R_{gb}$ ) and capacitance ( $C_g$  and  $C_{gb}$ ) were taken at a mega-ohm (M $\Omega$ ) and nano farad (nF) scale respectively. The constant phase element takes into account the departure from ideal Debye-like behaviour. The temperature dependent value of  $n$  varies between 0.275–0.406 (0.288–0.39) for BBT (BBT-TE) and 0.406–0.701 (0.497–0.564) for SBT (SBT-TE). The observed values of  $n$  indicate the CPE is neither purely resistive nor capacitive but a combination of both. The capacitance range for all samples obtained both below and above the transition temperature is in good agreement with the values of other ferroelectric systems.<sup>46</sup> The capacitance and resistance values indicate the samples are well sintered. Furthermore, the overall resistance was observed to be dominated by grains  $R_g$  at all temperatures.

The DC component of grain and grain boundary conductivities ( $\sigma_g \propto \frac{1}{R_g}, \sigma_{gb} \propto \frac{1}{R_{gb}}$ ) plotted with the inverse of temperature ( $T^{-1}$ ) is shown in Fig. 6.<sup>48</sup> These conductivities ( $\sigma_g$  and  $\sigma_{gb}$ ) follow the Arrhenius law,  $\sigma_g = \sigma_0 \exp\left(-\frac{E_g}{k_B T}\right)$  for grains and  $\sigma_{gb} = \sigma_0 \exp\left(-\frac{E_{gb}}{k_B T}\right)$  for grain boundaries, where  $\sigma_0$  is the pre-exponent factor,  $\sigma_g$  and  $\sigma_{gb}$  are the DC conductivities by grain and grain boundary respectively,  $E_g$  and  $E_{gb}$  are the activation energies of the grain and grain boundary respectively and  $k_B$  is the Boltzmann constant. The above equations are made linear by taking the natural log of both sides for easy interpretation.

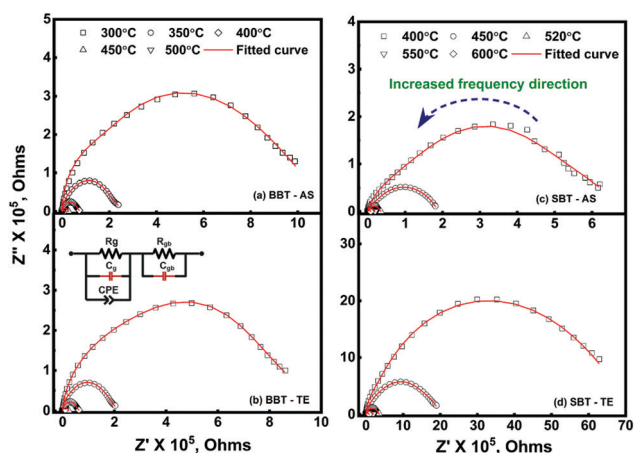


Fig. 5 The Nyquist plot ( $Z''$  vs.  $Z'$ ) for (a) BBT-AS, (b) BBT-TE, (c) SBT-AS and (d) SBT-TE. The equivalent circuit shown in the inset of (b) and the corresponding curve is used for fitting (red line) in the present study. The direction of the increase in frequency is presented in (c) with a blue dashed curved line.

Table 3 The extracted values of different elements of the equivalent circuit for BBT and SBT determined from fitting of the Nyquist plot. The values in parentheses belong to the TE pellet

Material name	Temp. (°C)	$R_g$ (M $\Omega$ )	$R_{gb}$ (M $\Omega$ )	$C_g$ (nF)	$C_{gb}$ (nF)	$n$
BBT	300	1 (0.796)	0.157 (0.211)	0.385 (0.136)	0.239 (0.275)	0.406 (0.39)
	350	0.191 (0.201)	0.0735 (0.0427)	0.318 (0.655)	2.039 (0.704)	0.372 (0.315)
	400	0.0571 (0.0478)	0.0206 (0.0182)	0.040 (0.044)	2.607 (2.913)	0.322 (0.331)
	450	0.0208 (0.0178)	0.0071 (0.0065)	0.865 (0.972)	0.389 (0.419)	0.275 (0.283)
	500	0.0089 (0.0066)	0.0029 (0.0038)	0.170 (0.856)	2.43 (0.023)	0.406 (0.335)
SBT	400	0.541 (6.987)	0.154 (0.474)	0.041 (0.015)	1.557 (0.037)	0.432 (0.552)
	450	0.167 (1.728)	0.014 (0.274)	0.093 (0.011)	0.161 (0.312)	0.613 (0.497)
	520	0.028 (0.338)	0.0075 (0.023)	0.752 (0.042)	0.432 (0.151)	0.406 (0.549)
	550	0.013 (0.17)	0.0057 (0.0285)	0.836 (0.044)	0.214 (0.043)	0.509 (0.564)
	600	0.0052 (0.071)	0.0023 (0.016)	0.147 (0.028)	0.141 (0.03)	0.701 (0.507)



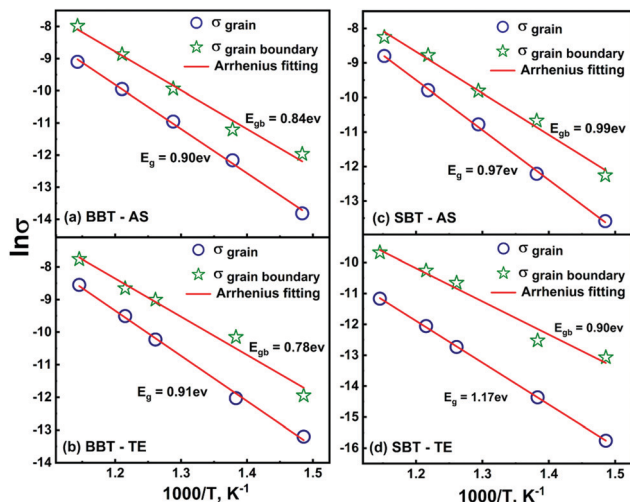


Fig. 6 The DC conductivities due to grain and grain boundary for (a) BBT-AS, (b) BBT-TE, (c) SBT-AS and (d) SBT-TE. The red line represents Arrhenius fitting.

The slope of linear fit is then used to obtain the activation energy.

The calculated values of activation energies of  $\sigma_g$  and  $\sigma_{gb}$  are  $E_g = 0.90$  eV,  $E_{gb} = 0.84$  eV for BBT-AS and  $E_g = 0.91$  eV and  $E_{gb} = 0.78$  eV for BBT-TE. However, the  $E_g$  and  $E_{gb}$  for SBT-AS (SBT-TE) are 0.97 eV (1.17 eV) and 0.99 eV (0.90 eV) respectively. This decrease in activation energy ( $\approx 0.01$  eV) of  $\sigma_{gb}$  in both complex oxides can be correlated with the improved homogeneity in the microstructure of thermally etched pellets. The bulk activation energy of  $\sigma_g$  for BBT remains nearly the same before and after heat treatment and shows an overall increase in the SBT. This is in good agreement with the decrease in dielectric constant post heat treatment in the SBT-TE samples. The temperature dependent values of dc conductivity, resistance and capacitance indicate that the overall dielectric properties are dominated by the bulk (grain) component in both BBT and SBT.

## 7 $P$ - $E$ hysteresis loop analysis

The room temperature ferroelectric behaviour of both the materials is illustrated in Fig. 7 with a hysteresis curve of polarization ( $P$ ) in the presence of an electric field ( $E$ ). The polling of the sample before studying ferroelectric behaviour in polycrystalline ceramics is a usual practice. However, this aligning of domains during the polling process dominates the overall polarization mechanism. Thus, to observe the contribution due to grains, grain boundaries and other polarization processes, the samples were not polled before the measurement in the present study. A clear hysteresis curve indicates a typical ferroelectric behaviour of Aurivillius oxides at room temperature.

The experimental polarization loops as a function of electric field were fitted with the following relation suggested by S. L. Miller<sup>49,50</sup> with an additional  $E$ -field independent loss term.<sup>51</sup>

$$P(E) = P_{\text{miller}} + P_{\text{loss}} \quad (7)$$

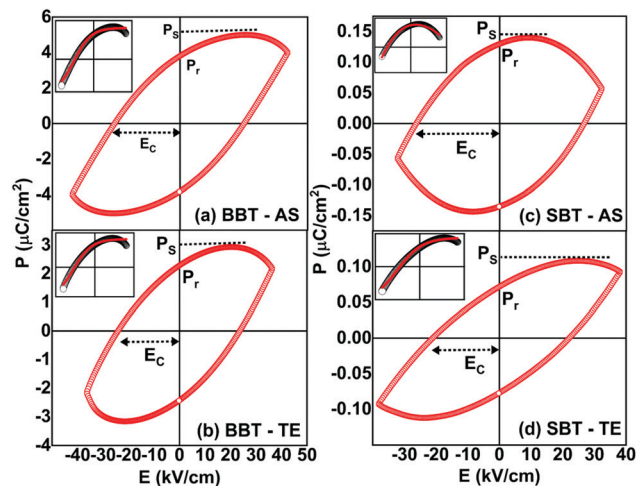


Fig. 7 The polarization  $P$  variation with electric field  $E$ , showing a ferroelectric hysteresis behaviour at room temperature for (a) BBT-AS, (b) BBT-TE, (c) SBT-AS and (d) SBT-TE. The inset of all the figures represents the upper half curve and the red line represents Miller fitting of the hysteresis curve.

and

$$P_{\text{miller}} = P_s \tanh \left[ \frac{(E - E_c)}{2\delta} \right] \quad (8)$$

therefore,

$$P(E) = P_s \tanh \left[ \frac{(E - E_c)}{2\delta} \right] + P_{\text{loss}} \quad (9)$$

where  $P_s$  and  $E_c$  are the saturation polarization and coercive electric field respectively.  $\delta$  is defined as:

$$\delta = E_c \left[ \log \left( \frac{1 + P_r/P_s}{1 - P_r/P_s} \right) \right] \quad (10)$$

The different values obtained by fitting polarization variation with the  $E$ -field are summarized in Table 4. To understand the contribution to polarization by various mechanisms, an approach suggested by H. Yan *et al.* is utilized.<sup>52</sup> In analogy to this model, the polarization in polycrystalline BBT and SBT shows a combined effect of contribution due to the dielectric constant, electric conductivity, and domain switching. The effect of non-ferroelectric components is clearly visible and evaluated by  $P_{\text{loss}}$ . The observed reduction in grain size post thermal etching is also evident in the  $P$ - $E$  loop with a smaller value of  $P_r$ . The heat treatment also slightly improves the texture, which can be seen by the lowering of the coercive field,

Table 4 The important parameters obtained by  $P$ - $E$  loop fitting for BBT and SBT

Sample-name	$P_s$	$\frac{P_r}{P_s}$	$E_c$	$P_{\text{loss}}$
BBT-AS	5.03	0.987	25.48	0.145
BBT-TE	3.12	0.99	25.03	0.259
SBT-AS	0.14543	0.998	26.13	$6 \times 10^{-5}$
SBT-TE	0.122	0.97	22.85	0.131



$E_C$ . All the  $P$ - $E$  curves are non-saturating and rounded; the non-saturating part is due to electrical permittivity, whereas the rounded curve is an indication of the conductivity contribution in agreement with Fig. 6. Furthermore, the loss factor in both thermally etched samples increases compared to the sintered counterparts. This is attributed to an increase in the grain boundary to grain ratio in the TE samples. The possibility of charge accumulation at the grain boundaries increases and hence contributes toward the losses.

## 8 Summary

In summary, single phase  $BaBi_4Ti_4O_{15}$  and  $SrBi_4Ti_4O_{15}$  have been synthesized and the effect of thermal etching on the structural, dielectric and piezoelectric properties was investigated. The room temperature X-ray diffraction and consequent Rietveld refinement confirms that all the synthesized Aurivillius compounds crystallize to the non-centrosymmetric orthorhombic (pseudo-tetragonal) phase with  $A2_1am$  symmetry. The microstructure shows a significant improvement post thermal etching, with a uniform grain size distribution and reduction in average grain size. However, the effect of this improvement in the microstructure is in contrast with the dielectric properties as the dielectric constant,  $\epsilon'$ , was observed to increase for  $BaBi_4Ti_4O_{15}$  and significantly reduce for  $SrBi_4Ti_4O_{15}$ . Furthermore, an appreciable difference in dielectric relaxation for complete substitution of the non-ferroelectric A-site in  $BaBi_4Ti_4O_{15}$  with Sr is surprising. The observed transition from the relaxor to ferroelectric phase and large change in transition temperature (from 400 °C to 521 °C) is attributed to the slightly different co-valency and electronic structure of two alkaline earth cations. The contribution due to grain (bulk) and grain boundary is evaluated using a brick-layer model. This model uses an equivalent circuit made of three sub-circuits representing the grain, grain boundary and constant phase element. The grain and grain boundary activation energy indicate that the electrical properties are dominated by grain (bulk) contribution and thus can be controlled by controlling its microstructure. The polarization variation with  $E$ -field is explained by a modified Miller expression. It is observed that a mechanism such as dielectric polarization and conductivity also contributes in addition to spontaneous polarization. The observed changes in ferroelectric parameters in thermally etched samples can be corroborated with the microstructure. Thus, the present study suggests that the macroscopic physical and transport properties are highly correlated and the desired properties can be tuned even by a simple single step processing parameter such as thermal etching in  $m = 4$  Aurivillius oxides  $[(Bi_2O_2)^{2+}[A_{m-1}B_mO_{3m+1}]^{2-}]$  ( $A = Ba, Sr$ ).

## Author contributions

SSR conceived the work and VKS carried out all the experimental work including synthesis of the samples and writing the original draft. RN and SSR analysed the data and wrote the final manuscript. All authors approved the final manuscript.

## Conflicts of interest

There are no conflicts to declare.

## Acknowledgements

The authors acknowledge the Science and Engineering Research Board (SERB), Govt. of India for financial support under sanctioned project no. ECR/2017/002691. The authors also acknowledge the Sophisticated Analytical Instrument Facility (SAIF), Manipal University Jaipur (MUJ) for the FESEM analysis, the User Facility at UGC DAE CSR, Indore for the X-ray diffraction measurements and the Indian Institute of Technology Bombay (IIT Bombay) for the Broadband Dielectric Spectroscopy (BDS) and PE loop measurements.

## Notes and references

- 1 N. Sezer and M. Koç, *Nano Energy*, 2021, **80**, 105567.
- 2 F. Narita and M. Fox, *Adv. Eng. Mater.*, 2018, **20**, 1700743.
- 3 A. Zaszczynska, A. Gradys and P. Sajkiewicz, *Polymers*, 2020, **12**, 2754.
- 4 B. C. Sekhar, B. Dhanalakshmi, B. S. Rao, S. Ramesh, K. V. Prasad, P. S. Rao and B. P. Rao, *Multifunctional Ferroelectric Materials*, Intech open, 2021, vol. 71, DOI: [10.5772/intechopen.92527](https://doi.org/10.5772/intechopen.92527).
- 5 D. Damjanovic, *Piezoelectric and acoustic materials for transducer applications*, Springer, 2008, pp. 59–79.
- 6 M. T. Chorsi, E. J. Curry, H. T. Chorsi, R. Das, J. Baroody, P. K. Purohit, H. Ilies and T. D. Nguyen, *Adv. Mater.*, 2019, **31**, 1802084.
- 7 J. Chen, Q. Qiu, Y. Han and D. Lau, *Renewable Sustainable Energy Rev.*, 2019, **101**, 14–25.
- 8 B. Narayan, J. S. Malhotra, R. Pandey, K. Yaddanapudi, P. Nukala, B. Dkhil, A. Senyshyn and R. Ranjan, *Nat. Mater.*, 2018, **17**, 427–431.
- 9 W. Qian, W. Yang, Y. Zhang, C. R. Bowen and Y. Yang, *Nano-Micro Lett.*, 2020, **12**, 1–39.
- 10 A. Aabid, B. Parveez, M. A. Raheman, Y. E. Ibrahim, A. Anjum, M. Hrairi, N. Parveen and J. Mohammed Zayan, *Actuators*, 2021, **10**(101), 1–26.
- 11 A. J. Bell, T. P. Comyn and T. J. Stevenson, *APL Mater.*, 2021, **9**, 010901.
- 12 W. H. Organization *et al.*, 2017.
- 13 A. Han, E. Han and E. Han *Hv*, 2011.
- 14 A. J. Bell and O. Deubzer, *MRS Bull.*, 2018, **43**, 581–587.
- 15 J. Koruza, A. J. Bell, T. Frömling, K. G. Webber, K. Wang and J. Rödel, *J. Materiomics*, 2018, **4**, 13–26.
- 16 H. Wei, H. Wang, Y. Xia, D. Cui, Y. Shi, M. Dong, C. Liu, T. Ding, J. Zhang and Y. Ma, *et al.*, *J. Mater. Chem. C*, 2018, **6**, 12446–12467.
- 17 F. Hussain, A. Khesro, Z. Lu, G. Wang and D. Wang, *Front. Mater.*, 2020, **7**, 87.
- 18 D. Maurya, M. Peddigari, M.-G. Kang, L. D. Geng, N. Sharpes, V. Annapureddy, H. Palneedi, R. Sriramdas, Y. Yan and H.-C. Song, *et al.*, *J. Mater. Res.*, 2018, **33**, 2235–2263.





- 19 N.-B. Do, H.-B. Lee, C.-H. Yoon, J.-K. Kang, J.-S. Lee and I.-W. Kim, *Trans. Electrical Electron. Mater.*, 2011, **12**, 64–67.
- 20 J. Wu, *J. Appl. Phys.*, 2020, **127**, 190901.
- 21 F. Hussain, A. Khesro, Z. Lu, G. Wang and D. Wang, *Front. Mater.*, 2020, **7**, 87.
- 22 T. Takenaka, K. Komura and K. Sakata, *Jpn. J. Appl. Phys.*, 1996, **35**, 5080.
- 23 H. Sun, Y. Wu, X. Xie, Y. Lu, T. Yao, J. Zhong and X. Chen, *J. Materiomics*, 2018, **4**, 353–359.
- 24 G. Nalini and T. G. Row, *Bull. Mater. Sci.*, 2002, **25**, 275–281.
- 25 B. J. Kennedy, Q. Zhou, Y. Kubota and K. Kato, *et al.*, *J. Solid State Chem.*, 2008, **181**, 1377–1386.
- 26 E. Subbarao, *J. Am. Ceram. Soc.*, 1962, **45**, 166–169.
- 27 C. H. Hervoches, A. Snedden, R. Riggs, S. H. Kilcoyne, P. Manuel and P. Lightfoot, *J. Solid State Chem.*, 2002, **164**, 280–291.
- 28 C. García de Andrés, F. Caballero, C. Capdevila and D. San Martín, *Mater. Charact.*, 2002, **49**, 121–127.
- 29 U. Täffner, V. Carle, U. Schäfer and M. J. Hoffmann, *Metallography and Microstructures*, ASM International, 2004.
- 30 J. Hu, X. Wang, J. Zhang, J. Luo, Z. Zhang and Z. Shen, *J. Materiomics*, 2021, **7**, 1007–1013.
- 31 T. Kimura, *J. Ceram. Soc. Jpn.*, 2016, **124**, 268–282.
- 32 L. K. Pradhan and M. Kar, author, 2021.
- 33 Y. Chen, K. H. Liu, Q. Luo, M. Mei, G. L. Chen, R. K. Pan, Y. J. Qi and W. Q. Cao, *J. Appl. Phys.*, 2019, **125**, 184104.
- 34 A. K. Jonscher, *J. Phys. D: Appl. Phys.*, 1999, **32**, R57–R70.
- 35 L. E. Cross, *Ferroelectrics*, 1987, **76**, 241–267.
- 36 T.-F. Zhang, X.-X. Huang, X.-G. Tang, Y.-P. Jiang, Q.-X. Liu, B. Lu and S.-G. Lu, *Sci. Rep.*, 2018, **8**, 1–12.
- 37 V. K. Sharma, R. Nathawat and S. S. Rathore, *2021 IEEE International Symposium on Applications of Ferroelectrics (ISAF)*, 2021, pp. 1–4.
- 38 M. Trainer, *Eur. J. Phys.*, 2000, **21**, 459–464.
- 39 D. Y. Suárez, I. M. Reaney and W. E. Lee, *MRS Online Proc. Libr.*, 2000, **658**, 1191–1196.
- 40 N. A. Benedek, J. M. Rondinelli, H. Djani, P. Ghosez and P. Lightfoot, *Dalton Trans.*, 2015, **44**, 10543–10558.
- 41 R. Machado, M. Stachiotti, R. Migoni and A. H. Tera, *Phys. Rev. B: Condens. Matter Mater. Phys.*, 2004, **70**, 214112.
- 42 A. Roy, R. Prasad, S. Auluck and A. Garg, *Appl. Phys. Lett.*, 2013, **102**, 182901.
- 43 S. Bobade, D. Gulwade, A. Kulkarni and P. Gopalan, *J. Appl. Phys.*, 2005, **97**, 074105.
- 44 A. Elbasset, S. Sayouri, F. Abdi, T. Lamcharfi and L. Mrharrab, *Glass Phys. Chem.*, 2017, **43**, 91–97.
- 45 S. Huang, C. Feng, L. Chen and Q. Wang, *J. Am. Ceram. Soc.*, 2006, **89**, 328–331.
- 46 J. T.-S. Irvine, D. C. Sinclair and A. R. West, *Adv. Mater.*, 1990, **2**, 132–138.
- 47 J.-B. Jorcin, M. E. Orazem, N. Pébère and B. Tribollet, *Electrochim. Acta*, 2006, **51**, 1473–1479.
- 48 R. Tang, C. Jiang, W. Qian, J. Jian, X. Zhang, H. Wang and H. Yang, *Sci. Rep.*, 2015, **5**, 13645.
- 49 S. L. Miller, R. D. Nasby, J. R. Schwank, M. S. Rodgers and P. V. Dressendorfer, *J. Appl. Phys.*, 1990, **68**, 6463–6471.
- 50 C. H. Tsang, C. K. Wong and F. G. Shin, *J. Appl. Phys.*, 2005, **98**, 084103.
- 51 K. Bhoi, H. Mohanty, M. F. Abdullah, D. K. Pradhan, S. N. Babu, A. Singh, P. Vishwakarma, A. Kumar, R. Thomas and D. K. Pradhan, *et al.*, *Sci. Rep.*, 2021, **11**, 1–17.
- 52 H. Yan, F. Inam, G. Viola, H. Ning, H. Zhang, Q. Jiang, T. Zeng, Z. Gao and M. J. Reece, *J. Adv. Dielectr.*, 2011, **01**, 107–118.

